Frontiers in Bioscience Landmark

Front. Biosci. (Landmark Ed) **2026**; 31(7): 51583
https://doi.org/10.31083/FBL51583

Original Research

The miR-339-5p/ACSL4 Pathway Drives Ferroptosis in Macrophages Exposed to Silica Nanoparticles

Wanxin Zhang[1], Yanbo Li[2], Zhongjun Du[3,*], Hua Shao[1,3,*]

[1]College of Traditional Chinese Medicine, Shandong University of Traditional Chinese Medicine, 250335 Jinan, Shandong, China
[2]Department of Toxicology and Sanitary Chemistry, School of Public Health, Capital Medical University, 100069 Beijing, China
[3]Department of Toxicology, Shandong Academy of Occupational Health and Occupational Medicine, Shandong First Medical University & Shandong Academy of Medical Sciences, 250062 Jinan, Shandong, China
*Correspondence: duzhongjun@sdfmu.edu.cn (Zhongjun Du); chinashaohua5888@163.com (Hua Shao)
Academic Editor: Sung Eun Kim
Submitted: 6 March 2026 Revised: 14 May 2026 Accepted: 3 June 2026 Published: 24 July 2026

Abstract

Background: The widespread application of silica nanoparticles (SiNPs) in industrial fields has raised increasing concerns regarding their potential biological toxicity. However, the cellular mechanisms underlying SiNPs-related injury remain incompletely understood. This study was designed to investigate whether ferroptosis contributes to SiNPs-mediated cytotoxicity in macrophages and to explore the potential regulatory role of microRNAs. **Methods:** RAW264.7 cells were exposed to SiNPs to establish an *in vitro* toxicity model. Mitochondrial ultrastructure and cellular uptake were examined. Ferroptosis-related markers, including antioxidant capacity, lipid peroxidation, ferrous iron accumulation, and the expression of glutathione peroxidase 4 (GPX4), acyl-CoA synthetase long-chain family member 4 (ACSL4), and cyclooxygenase-2 (COX2), were assessed. The involvement of apoptosis and necroptosis was evaluated using specific pathway inhibitors. Transcriptomic sequencing was performed to identify differentially expressed miRNAs, followed by functional validation through miR-339-5p mimic transfection, and the direct interaction between miR-339-5p and ACSL4 was verified by dual luciferase reporter assay. **Results:** SiNPs were efficiently internalized by RAW264.7 cells and induced pronounced mitochondrial structural damage, characterized by mitochondrial shrinkage and loss of cristae. SiNPs exposure markedly impaired cellular antioxidant capacity and promoted the accumulation of lipid peroxides and intracellular Fe^{2+}. This coincided with a reduction in GPX4 expression, whereas ACSL4 and COX2 levels increased. Ferroptosis was identified as the predominant mode of SiNPs-induced cytotoxicity, while apoptosis and necroptosis played minor roles. Transcriptomic analysis identified miR-339-5p as a potential regulator associated with ferroptosis-related pathways, and the dual luciferase reporter assay confirmed that miR-339-5p directly targets *Acsl4*. Overexpression of miR-339-5p significantly attenuated the ferroptosis response induced by SiNPs. **Conclusions:** SiNPs induce ferroptosis as the predominant mode of cell death in macrophages through mechanisms involving oxidative stress and lipid peroxidation. miR-339-5p acts as a negative regulator of this process by directly targeting ACSL4, alleviating ferroptotic injury and providing new insights into the molecular mechanisms underlying the toxicity of SiNPs.

Keywords: silicon dioxide; nanoparticles; macrophages; ferroptosis; microRNAs

1. Introduction

SiNPs represent a class of silica particles characterized by dimensions in the nanometer range, typically spanning from 1 to 100 nanometers [1,2]. The appeal of SiNPs lies in their exceptional physicochemical profile, encompassing an elevated surface-to-volume ratio, a precisely engineered and adjustable porous architecture, as well as optical characteristics that can be readily modulated to meet specific application requirements [3]. Owing to these unique characteristics, SiNPs have emerged as one of the extensively employed and manufactured nanomaterials, and have been applied across the food, cosmetics, decorative materials, and pest control industries, among others [4,5,6]. The sub-100 nm diameter of SiNPs enables them to enter the human body via multiple pathways, including respiratory inhalation, oral ingestion, and dermal absorption, with inhalation constituting the predominant mode of occupational exposure [7,8]. Current evidence supports the potential toxicity of these SiNPs, which can penetrate the lungs via the respiratory tract, depositing in the alveoli and eliciting an inflammatory response [9,10]. Prolonged exposure to high concentrations of SiNPs has been linked to the development of pulmonary fibrosis (PF) [11,12]. The International Agency for Research on Cancer (IARC) has categorized amorphous silica under Group 3, denoting inadequate evidence of carcinogenicity, while crystalline silica falls under Group 1, meaning it is confirmed as being carcinogenic to humans. Owing to their small size and extensive surface area, the toxicity of SiNPs may surpass that of crystalline silica [13]. In light of this potential risk, SiNPs have been designated by the Organization for Economic Cooperation and Development as a priority substance for toxicity assessment [14]. Elucidating the mechanisms underlying SiNPs-induced lung injury is therefore critical for assessing any associated health risks.

Mounting evidence substantiates the pivotal role of macrophages in the pathogenesis of lung injury and PF [15,16,17,18]. Located at the critical interface between the airway lumen and the alveolar space, alveolar macrophages serve as the primary cellular defenders of the respiratory tract by actively eliminating inhaled particles to preserve tissue homeostasis [19,20]. Inhaled SiNPs can penetrate deeply into the lungs and accumulate within the alveolar region, as primary sentinels of pulmonary immunity, alveolar macrophages respond to SiNP deposition through active phagocytosis, setting in motion a series of clearance processes that collectively attenuate lung injury [21,22]. Typically, in cases of lung tissue invasion, SiNPs are phagocytosed by macrophages [23,24]. These macrophages often fail to effectively degrade SiNPs. However, the intracellular accumulation of these particles inflicts cellular injury or death, consequently triggering the release of a cascade of pro-inflammatory and pro-fibrotic mediators [25,26]. The released SiNPs are, in turn, captured by other macrophages, perpetuating this deleterious cycle and ultimately contributing to the development of PF.

Recent studies have established a correlation between macrophage apoptosis, autophagy, and the progression of PF [27,28]. Ferroptosis is a molecularly distinct mode of cell death, bearing hallmark characteristics that set it apart from classical death pathways such as apoptosis, necrosis, and autophagy [29]. Ferroptosis is defined by the intracellular accumulation of lipid-derived reactive oxygen species alongside characteristic ultrastructural mitochondrial changes, including membrane condensation, organelle rounding, and loss of cristae, and has been increasingly implicated in a spectrum of pathological conditions such that it holds immense promise attracting growing attention as a novel target for disease treatment [30]. A growing body of evidence further suggests that the dysregulation of pulmonary iron homeostasis is closely linked to both the initiation and progression of PF [31,32]. Pulmonary macrophages derived from PF patients display increased intracellular iron accumulation accompanied by enhanced iron-mediated oxidative radical generation [33].

Macrophage-secreted miRNAs have been increasingly implicated as key regulators of the pathogenesis of PF [34]. miRNAs are a class of small non-coding RNAs that serve as pivotal post-transcriptional regulators that govern gene expression and, in turn, modulate key cellular processes including proliferation and cell death [35]. Notably, certain miRNAs, such as miR-486-5p, miR-130b-3p, and miR-let-7, have been identified as regulators of ferroptosis [36,37,38].

In this study, RAW264.7 macrophages were used as an *in vitro* model to characterize the mechanistic link between SiNPs exposure and ferroptosis activation, with a particular emphasis on the regulatory role of miRNAs. Ferroptosis-associated markers were systematically assessed, and transcriptomic sequencing was performed to identify and functionally characterize ferroptosis-related miRNAs in the context of SiNPs exposure. Together, these analyses led to the identification of miR-339-5p as a key regulator of SiNPs-induced ferroptosis in RAW264.7 cells, shedding new light on the molecular mechanisms underlying the toxicity of SiNPs and highlighting potential avenues for therapeutic intervention.

2. Materials and Methods

2.1 Characterization of SiNPs

SiNPs (SISN50, nanoComposix, San Diego, CA, USA) with a nominal size of 50 nm were thoroughly dispersed by ultrasonication for 20 min. An aliquot of the resulting suspension was then dropped onto a carbon-coated copper grid and air-dried prior to observation by transmission electron microscopy (TEM).

2.2 Cell Culture

RAW264.7 cells, obtained from the Cell Bank of the Chinese Academy of Sciences Type Culture Collection, were maintained in high-glucose DMEM (C11995500BT, Gibco, Waltham, MA, USA) supplemented with 10% fetal bovine serum (FBS; 10099-141, Gibco, Melbourne, VIC, Australia) and 1% penicillin-streptomycin (15140122, Gibco, Waltham, MA, USA). Cells were cultured at 37 °C in a humidified incubator with 5% CO_2, subculturing was performed every 2–3 days, and only cells in the logarithmic growth phase were used for experiments. Cells were seeded at 1×10^4 cells per well in 96-well plates for cell viability assays, and 5×10^5 cells per well in 6-well plates for transfection, Western blot, and other functional assays. Cells between passages P3–P8 were used for all experiments. RAW264.7 cells were authenticated by short tandem repeat (STR) profiling and tested negative for mycoplasma contamination.

2.3 Cell Viability Assay

RAW264.7 cells were seeded into 96-well culture plates and exposed to varying concentrations of SiNPs (0, 6.25, 12.5, 25, 50, and 100 μg/mL) for 3, 6, 12, and 24 h. Cell viability was assessed using the Cell Counting Kit-8 (CCK-8; CK04, Dojindo Molecular Technologies, Kumamoto, Japan) according to the manufacturer's instructions, with absorbance measured at 450 nm using a microplate reader.

To investigate the involvement of ferroptosis, apoptosis, and necroptosis in SiNPs-induced cell death, RAW264.7 cells were pretreated for 2 h prior to SiNPs exposure with Ferrostatin-1 (Fer-1; S7243, Selleck Chemicals, Houston, TX, USA), a selective ferroptosis inhibitor; Z-VAD-FMK (Z-VAD; S7023, Selleck Chemicals, Houston, TX, USA), a pan-caspase inhibitor that blocks apoptosis; or Necrostatin-1 (Nec-1; S8037, Selleck Chemicals, Houston, TX, USA), an inhibitor of necroptosis. All inhibitors were dissolved in dimethyl sulfoxide to prepare 10

mM stock solutions, which were further diluted with serum-free high-glucose DMEM to final concentrations of 10 μM prior to use, respectively. These concentrations were selected based on previous studies and our preliminary experiments, which demonstrated effective inhibition of the respective cell death pathways without inducing cytotoxicity [39]. The final concentration of DMSO in all treatment groups did not exceed 0.1% (v/v). Cells were then seeded into 96-well culture plates and exposed to SiNPs at 50 μg/mL for 12 h. Cell viability was assessed using the CCK-8 assay as described above.

2.4 ROS Measurement

Lipid reactive oxygen species (ROS) levels in RAW264.7 cells were evaluated using the BODIPY™ 581/591 C11 probe (D3861, Thermo Fisher Scientific, Waltham, MA, USA) according to the manufacturer's protocol. Briefly, cells were seeded in 6-well plates and exposed to varying concentrations of SiNPs for 12 h. After treatment, cells were incubated with the BODIPY™ probe for 30 min, then harvested using TrypLE™ Express Enzyme (TrypLE; 12604013, Gibco, Waltham, MA, USA) and rinsed once with Hanks' Balanced Salt Solution (HBSS; 14025092, Gibco, Waltham, MA, USA). Fluorescence signals were subsequently acquired on a DxFLEX Flow Cytometer (Beckman Coulter, Brea, CA, USA). Flow cytometry data were analyzed by first gating the main cell population based on forward scatter (FSC) and side scatter (SSC) characteristics to exclude cellular debris. Intracellular lipid ROS levels were then quantified by measuring the fluorescence intensity of BODIPY™ 581/591 C11 in the gated cell population.

2.5 MDA Assay

Malondialdehyde (MDA) levels were measured using a thiobarbituric acid (TBA)-based assay kit (S0131S, Beyotime Biotechnology, Shanghai, China) according to the manufacturer's instructions. Briefly, a TBA stock solution was prepared and fully dissolved by heating at 70 °C if necessary, followed by storage at room temperature protected from light. An MDA working solution was freshly prepared before use. Standard solutions (1, 2, 5, 10, 20, and 50 μM) were prepared by diluting the provided standard with distilled water to generate a standard curve. After treatment, samples were processed according to the kit protocol, and the absorbance was measured at 532 nm using a microplate reader. MDA levels were calculated based on the standard curve.

2.6 Fe^{2+} Fluorescence Assay

Intracellular ferrous iron (Fe^{2+}) levels were measured using FerroOrange (F374, Dojindo Molecular Technologies, Kumamoto, Japan). RAW264.7 cells were seeded into black 96-well plates and treated as indicated for 12 h. After treatment, cells were washed once with phosphate-buffered saline (PBS). Cells were first incubated with Hoechst 33258 (C1017, Beyotime Biotechnology, Shanghai, China) for 10 min to stain nuclei. After removal of the dye, cells were incubated with 1 μM FerroOrange at 37 °C for 30 min in the dark. Fluorescence intensity was immediately measured using a fluorescence microplate reader (BMG LABTECH, Ortenberg, Germany). The ratio of FerroOrange fluorescence intensity to Hoechst 33258 fluorescence intensity was calculated to represent intracellular Fe^{2+} levels.

2.7 Transmission Electron Microscopy (TEM)

To assess cellular uptake of SiNPs and subsequent ultrastructural alterations, RAW264.7 cells were exposed to 50 μg/mL SiNPs for 12 h. Cells were then harvested using TrypLE, pelleted by centrifugation (800 rpm, 4 min), and fixed with glutaraldehyde fixative at 4 °C for 6 h. After three rinses with distilled water, samples were dehydrated through a graded ethanol series (15 min per step), infiltrated with a propylene oxide-resin mixture (1:4 ratio), and embedded. Ultrathin sections were prepared using an ultramicrotome, stained with uranyl acetate for 10 min, and examined via TEM.

2.8 RNA Extraction

Total RNA was extracted from RAW264.7 cells using the SPARKeasy Improved Cell RNA Kit (AC0205, SparkJade Biotechnology, Qingdao, China) according to the manufacturer's instructions. RNA integrity and purity were then evaluated using a NanoDrop2000 spectrophotometer (Thermo Fisher Scientific, Waltham, MA, USA).

2.9 miRNA Sequencing and Analysis

RAW264.7 cells were subjected to SiNPs treatment to induce ferroptosis, after which total RNA was isolated using the mirVana miRNA Isolation Kit (AM1561, Ambion, Thermo Fisher Scientific, Austin, TX, USA) according to the manufacturer's protocol. RNA concentration was determined using a NanoDrop 2000 spectrophotometer, and RNA integrity was assessed on an Agilent 2100 Bioanalyzer (Agilent Technologies, Santa Clara, CA, USA). Library quality was subsequently confirmed using the same Agilent 2100 platform.

2.10 Bioinformatics Analyses

Raw sequencing reads were subjected to quality control to filter out low-quality reads and those containing poly(A) sequences. After aligning the clean reads to the reference genome, miRNA expression levels were normalized for cross-sample comparability. Differentially expressed miRNAs (DEMs) were identified based on the following criteria: q-value < 0.05 and fold change (FC) >2 or <0.5. To explore the functional roles of predicted DEM target genes, Gene Ontology (GO) and Kyoto Encyclopedia of Genes and Genomes (KEGG) pathway enrichment analyses were performed. Significantly enriched GO terms and KEGG pathways were defined by an adjusted p-value < 0.05.

2.11 Real-Time Quantitative Polymerase Chain Reaction Verification

To validate the sequencing results, miR-339-5p expression was quantified by quantitative real-time PCR (qRT-PCR). Total RNA was extracted from RAW264.7 cells treated with or without SiNPs (50 μg/mL, 12 h), and reverse transcription was performed using the HiScript II 1st Strand cDNA Synthesis Kit (+gDNA wiper) (R212, Vazyme Biotech, Nanjing, China). qRT-PCR was then carried out on a Roche LightCycler® 480 II System (Roche, Basel, Switzerland) according to the manufacturer's protocol. Relative miRNA expression levels were calculated using the $2^{-\Delta\Delta Ct}$ method. The primer sequences used for qRT-PCR were synthesized by GenePharma (Shanghai, China) and were as follows: mmu-miR-339-5p forward (F), 5′-TCTGTCTATCCCTGTCCTCCAG-3′ and reverse (R), 5′-AATGGTTGTTCTCCACTCTCTCTC-3′; U6 snRNA forward (F), 5′-CGCTTCGGCAGCACATATAC-3′ and reverse (R), 5′-TTCACGAATTTGCGTGTCATC-3′.

2.12 miR-339-5p Mimics Transfection

After appropriate cell plating, the culture medium was exchanged for a transfection mixture containing 5 μL of either miR-339-5p mimics (GenePharma, Shanghai, China) or the corresponding negative control (GenePharma, Shanghai, China), 3 μL of Lipofectamine 3000 (L3000008, Invitrogen, Thermo Fisher Scientific, Waltham, MA, USA), 250 μL of OptiMEM (31985062, Gibco, Waltham, MA, USA), and 4 mL of high glucose DMEM per well and incubated for 24 h. The miR-339-5p mimics and negative control oligonucleotides were synthesized by GenePharma (Shanghai, China). The sequences were as follows: mmu-miR-339-5p mimics sense, 5′-UCCCUGUCCUCCAGGAGCUCACG-3′ and antisense, 5′-UGAGCUCCUGGAGGACAGGGAUU-3′; negative control sense, 5′-UUCUCCGAACGUGUCACGUTT-3′ and antisense, 5′-ACGUGACACGUUCGGAGAATT-3′. RT-qPCR was then carried out to evaluate the expression of miR-339-5p in these transfected cells as a readout for transfection efficiency.

2.13 Western Blotting

Proteins were extracted from cells using RIPA lysis buffer (P0013B, Beyotime Biotechnology, Shanghai, China). Equal amounts of protein (20 μg) were separated by 10% SDS-PAGE and transferred to PVDF membranes (ISEQ00010, Merck Millipore, Burlington, MA, USA), followed by blocking with 5% skim milk. Membranes were incubated overnight at 4 °C with the following primary antibodies: mouse TFRC (13-6800, dilution 1:1000; Invitrogen, Thermo Fisher Scientific, Waltham, MA, USA), rabbit COX2 (12282S, dilution 1:1000; Cell Signaling Technology, Danvers, MA, USA), rabbit ACSL4 (ab155282, dilution 1:10,000; Abcam, Cambridge, UK), rabbit GCLC (12601-1-AP, dilution 1:1000; Proteintech, Wuhan, China), rabbit XCT (ab175186, dilution 1:1000; Abcam, Cambridge, UK), rabbit RPL8 (ab169538, dilution 1:10,000; Abcam, Cambridge, UK), rabbit GPX4 (ab125066, dilution 1:1000; Abcam, Cambridge, UK), rabbit FTH1 (4393S, dilution 1:1000; Cell Signaling Technology, Danvers, MA, USA), rabbit Caspase3 (19677-1-AP, dilution 1:1000; Proteintech, Wuhan, China), rabbit MLKL (21066-1-AP, dilution 1:1000; Proteintech, Wuhan, China), rabbit p-MLKL (abs130437, dilution 1:1000; Abmart, Shanghai, China) and rabbit β-actin (4970S, dilution 1:1000; Cell Signaling Technology, Danvers, MA, USA). After washing, membranes were incubated with IRDye® 680RD goat anti-rabbit IgG (926-68071, dilution 1:10,000; LI-COR Biosciences, Lincoln, NE, USA) for rabbit primary antibodies, or IRDye® 800CW goat anti-mouse IgG (926-32210, dilution 1:10,000; LI-COR Biosciences, Lincoln, NE, USA) for the mouse primary antibody. β-Actin was used as an internal loading control for normalization, and immunoreactive bands were quantified using ImageJ software (version 1.53, National Institutes of Health, Bethesda, MD, USA).

2.14 Dual Luciferase Reporter Assay

The wild-type (WT) and mutated (Mut) 3′untranslated region (UTR) sequences of *Acsl4* were cloned into luciferase reporter vectors. 293T cells were co-transfected with miR-339-5p mimics or negative control (NC) constructs together with the respective reporter constructs using Lipofectamine 2000 (11668019, Invitrogen, Thermo Fisher Scientific, Waltham, MA, USA) according to the manufacturer's instructions. Each group treatment was performed in triplicate. At 48 h post-transfection, cells were washed with PBS, lysed with lysis buffer at room temperature for 15 min, and centrifuged at 12,000 ×g for 2 min at 4 °C. Firefly and Renilla luciferase activity levels were then measured sequentially using the Dual Luciferase Reporter Gene Assay Kit (11402ES60, Yeasen Biotechnology, Shanghai, China) on a GloMax 20/20 luminometer (Promega Corporation, Madison, WI, USA). Relative luciferase activity was expressed as the ratio of Firefly to Renilla luciferase activity, and data are presented as mean ± standard deviation (SD). 293T cells were authenticated by short tandem repeat (STR) profiling and tested negative for mycoplasma contamination.

2.15 Statistical Analysis

All data, obtained from at least three independent experiments, are presented as mean ± SD. Data normality and homogeneity of variance were assessed using the Shapiro–Wilk test and Levene's test, respectively, prior to parametric analyses. Statistical analyses were performed using GraphPad Prism (Version 9.0, GraphPad Software, San Diego, CA, USA). Two-group comparisons were analyzed using Student's two-tailed *t*-test, while one-way or two-way analysis of variance (ANOVA) followed by Bonferroni's post-hoc test was used for multiple-group comparisons. For se-

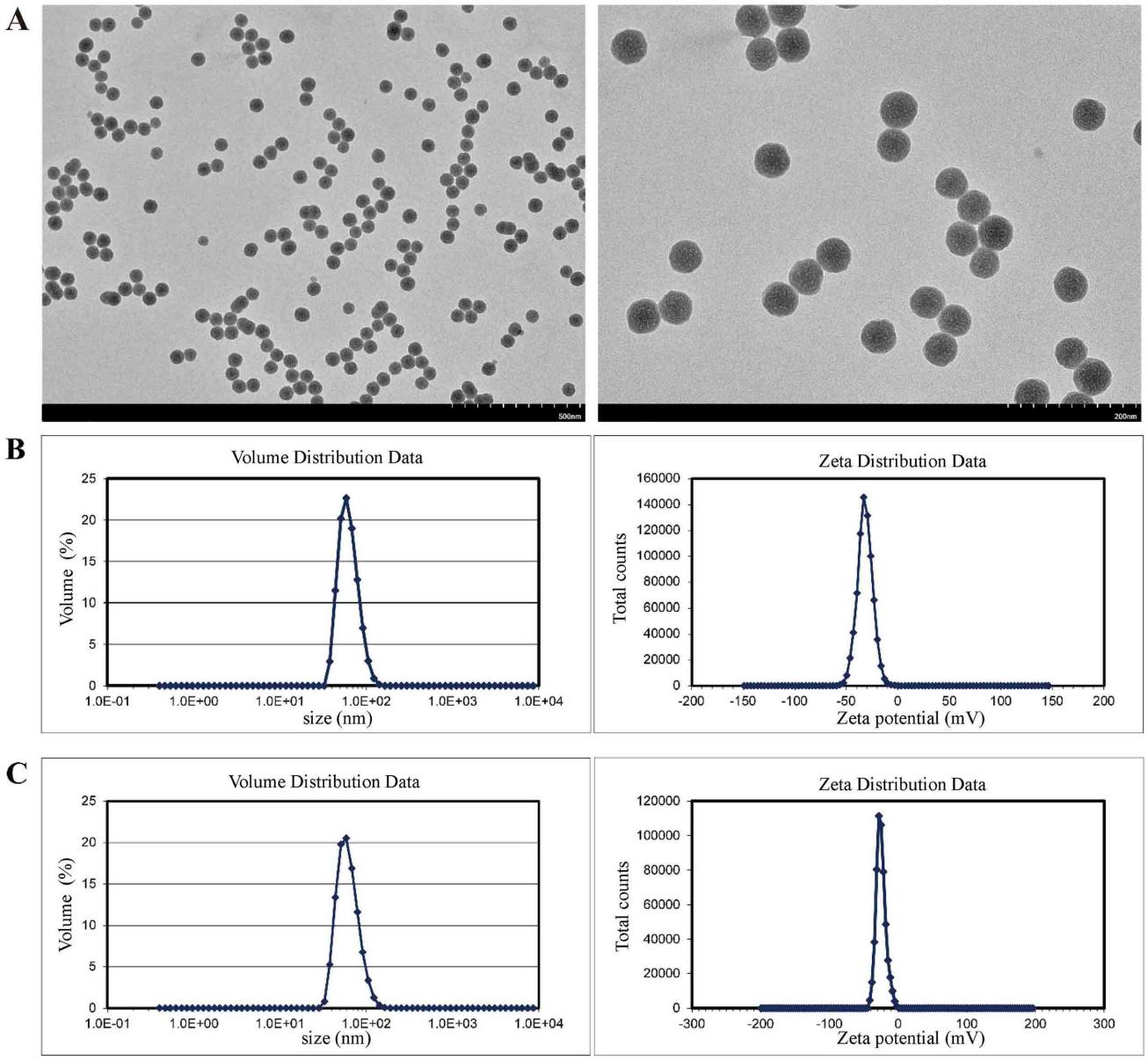

Fig. 1. Characterization of SiNPs. (A) TEM images showing the morphology and size distribution of SiNPs (scale bar: 500 nm, left; 200 nm, right). (B,C) Volume distribution and zeta potential of SiNPs dispersed in distilled water (B) and high-glucose DMEM (C).

quencing data, differentially expressed miRNAs were identified using DESeq2. p-value < 0.05 was considered statistically significant.

3. Results

3.1 Characterization of SiNPs

The morphological features of SiNPs were characterized by TEM, revealing uniformly spherical nanoparticles under varying magnifications. Two hundred particles were examined using the ImageJ software, revealing an average particle size of 48.94 ± 2.60 nm, consistent with the 50 nm particle size indicated by the manufacturer (Fig. 1A).

Zeta potential is a key indicator of dispersion stability, with higher absolute values reflecting a more stable system. In pure water, the hydrodynamic diameter of the SiNPs was measured at 70.12 ± 0.62 nm, accompanied by a zeta potential of –31.03 ± 0.36 mV (Fig. 1B). In high glucose DMEM, the hydrodynamic diameter of these particles was recorded at 71.92 ± 0.16 nm, with a corresponding zeta potential of –24.93 ± 0.31 mV (Fig. 1C). These data suggest that SiNPs are uniformly distributed in pure water and high-glucose DMEM, with good dispersibility (Table 1).

3.2 SiNPs Induce Oxidative Stress in RAW264.7 Cells

To evaluate the cytotoxic effects of SiNPs, RAW264.7 cells were incubated with increasing concentrations of SiNPs (6.25, 12.5, 25, 50, and 100 μg/mL) for 3, 6, 12, and 24 h. CCK-8 cell viability assays revealed a time- and

Table 1. Hydrodynamic diameter and zeta potential of SiNPs in different media.

Group	Hydrodynamic diameter (nm)	Zeta potential (mV)
Distilled water	70.12 ± 0.62	–31.03 ± 0.36
High-glucose DMEM	71.92 ± 0.16	–24.93 ± 0.31

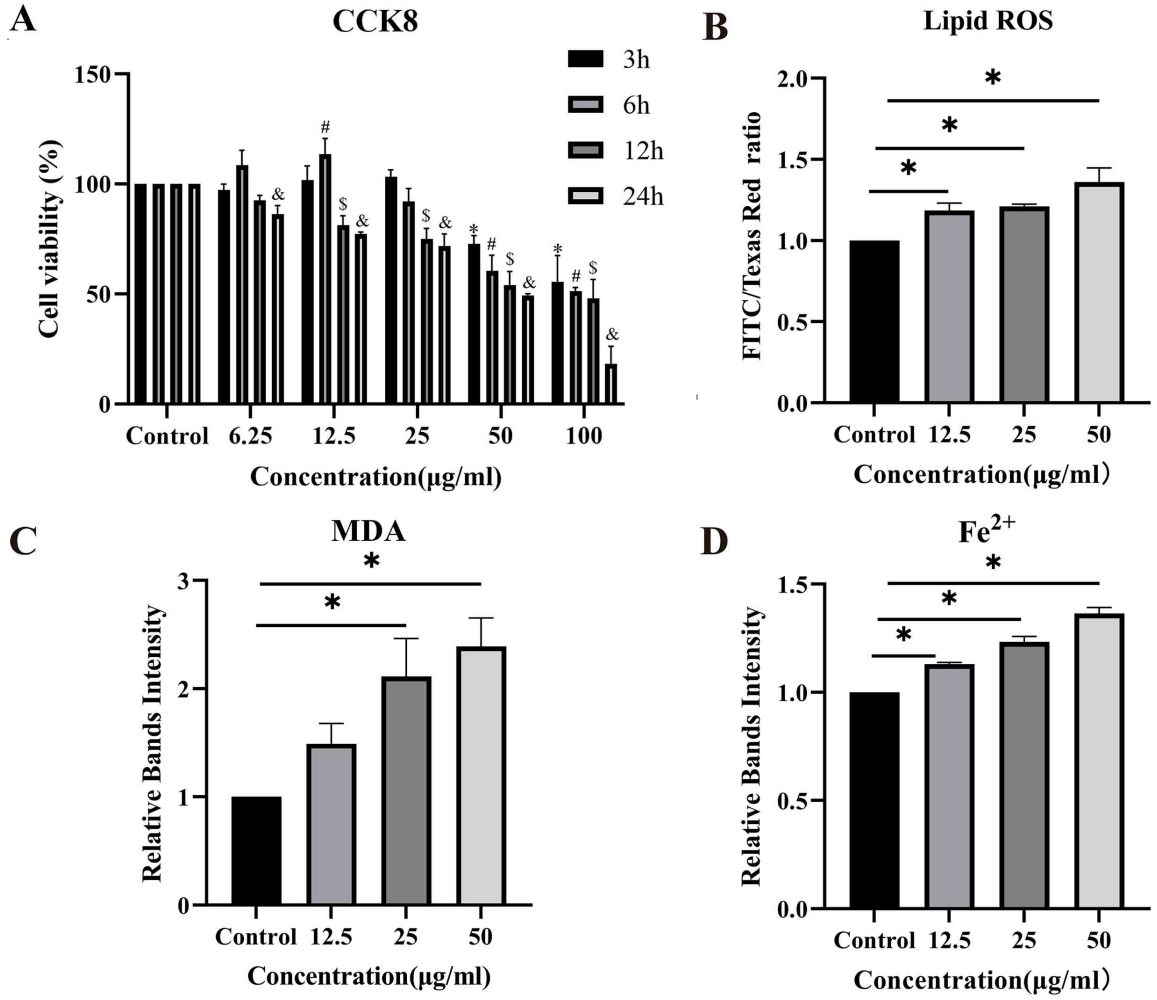

Fig. 2. Cytotoxic effects of SiNPs on RAW264.7 cells. (A) CCK-8 assay-based analysis of the viability of RAW264.7 cells exposed to different concentrations of SiNPs for 3, 6, 12, and 24 h. (B) Lipid ROS levels in cells treated with SiNPs for 12 h, expressed as the FITC/Texas Red fluorescence ratio. (C,D) MDA and Fe^{2+} levels in cells treated with SiNPs for 12 h. Cell viability data (A) were analyzed using two-way ANOVA followed by Bonferroni's post-hoc test. $^{*}p < 0.05$ *vs.* 3 h control; $^{\#}p < 0.05$ *vs.* 6 h control; $^{\$}p < 0.05$ *vs.* 12 h control; $^{\&}p < 0.05$ *vs.* 24 h control. Data in (B–D) were analyzed using one-way ANOVA followed by Bonferroni's post-hoc test; $^{*}p < 0.05$ *vs.* control group.

dose-dependent decline in survival at 12 and 24 h, whereas no clear dose dependence was observed at 3 or 6 h (Fig. 2A). Two-way ANOVA revealed significant effects of SiNP concentration and exposure time on RAW264.7 cell viability, as well as a significant interaction between concentration and exposure time (interaction: $F(15, 48) = 7.650$, $p < 0.0001$). Based on these observations, SiNPs concentrations of 12.5, 25, and 50 μg/mL and a 12 h exposure time were selected for subsequent mechanistic studies.

Analysis of intracellular Fe^{2+}, ROS, and MDA levels in these treated macrophages revealed significant, dose-dependent increases in SiNPs-treated cells (Fig. 2B–D), indicating elevated levels of lipid peroxidation. The concurrent accumulation of labile iron and ROS suggests that SiNPs disrupt iron homeostasis and redox balance, key biochemical events driving ferroptosis.

3.3 SiNPs Induce Mitochondrial Abnormalities in RAW264.7 Cells

TEM imaging demonstrated the ability of RAW264.7 cells to efficiently internalize SiNPs (Fig. 3A,B). Upon exposure, mitochondria in these cells displayed marked struc-

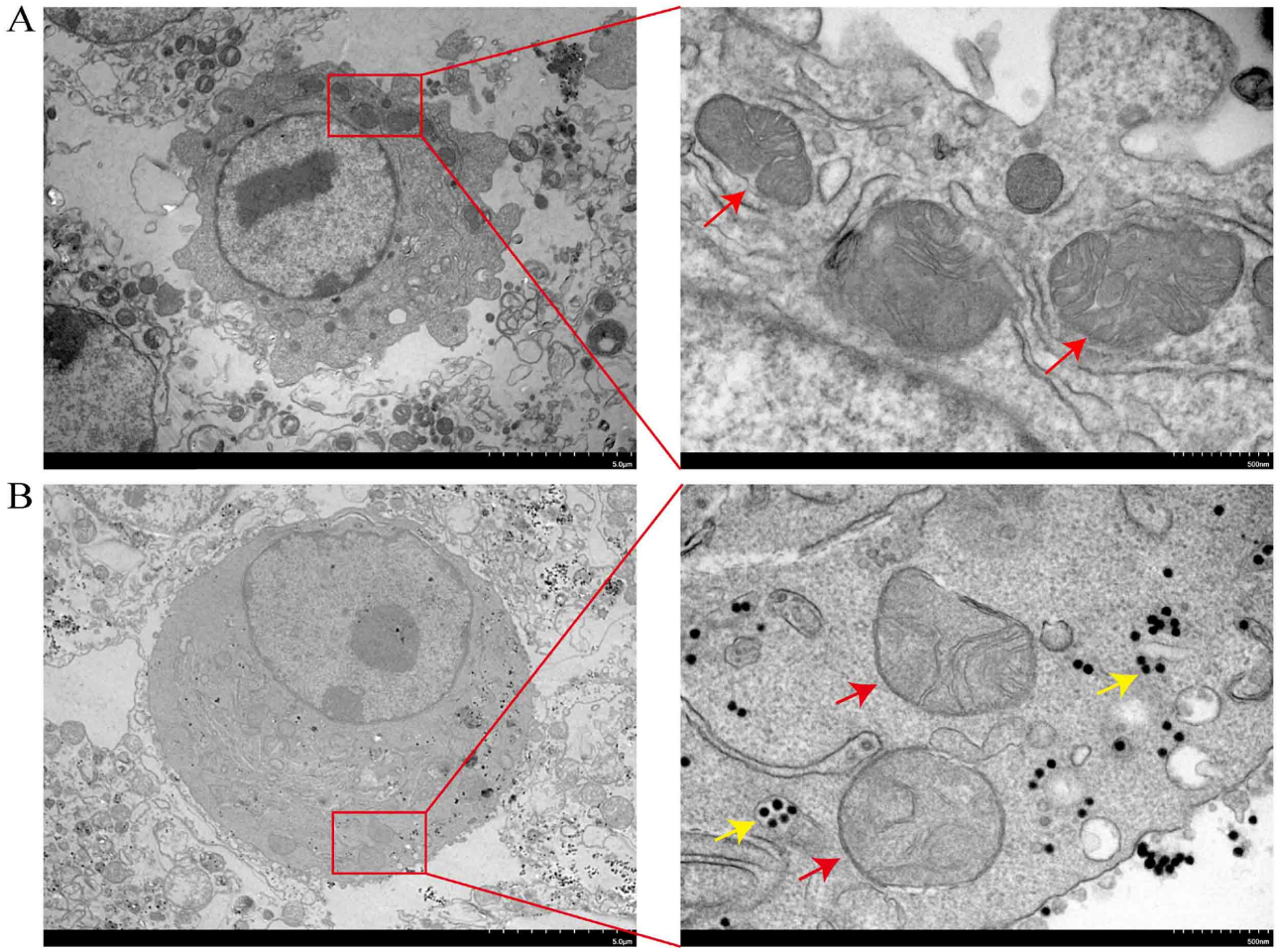

Fig. 3. SiNPs induce mitochondrial abnormalities in RAW264.7 cells. (A) Transmission electron microscopy (TEM) images of control cells showing normal mitochondrial morphology with intact cristae (red arrows) (scale bar: 5 µm, left; 500 nm, right). (B) TEM images of SiNPs-treated cells showing internalized SiNPs (yellow arrows) and mitochondria with characteristic ferroptotic changes, including shrinkage, increased membrane density, and reduced or vanished cristae (red arrows) (scale bar: 5 µm, left; 500 nm, right).

tural alterations, including pronounced shrinkage, rounding, and loss of cristae. These changes are characteristic of early ferroptosis events and indicate compromised mitochondrial integrity. The observed morphological defects suggest impaired bioenergetic function, which may facilitate the accumulation of labile iron and ROS, thereby promoting lipid peroxidation.

3.4 SiNPs Trigger Ferroptotic Signaling in RAW264.7 Cells

Western blotting demonstrated that exposure to SiNPs markedly altered the expression of key regulators of ferroptosis in RAW264.7 cells (Fig. 4). GPX4, the central glutathione peroxidase responsible for lipid hydroperoxide detoxification, was significantly downregulated, accompanied by a decrease in FTH1, the predominant intracellular iron storage protein, and TFRC, the membrane receptor that facilitates transferrin-mediated iron internalization. These findings indicate dysregulation of intracellular iron homeostasis and impairment of antioxidant defense systems. In parallel, the ferroptosis effectors ACSL4 and COX2 were markedly upregulated in these cells, reflecting enhanced lipid peroxidation and membrane susceptibility to oxidative damage. Notably, the observed upregulation of GCLC and xCT, which are components of the glutathione synthesis and cystine/glutamate antiporter systems, likely represents a compensatory cellular response to counteract oxidative stress. Collectively, these coordinated changes in antioxidant and ferroptosis proteins indicate that SiNPs trigger ferroptosis in RAW264.7 cells through the dysregulation of iron metabolism and amplification of lipid peroxidation.

3.5 Fer-1 Attenuates SiNPs-Induced Cell Injury Via Inhibiting Ferroptosis

Next, Fer-1 was administered to RAW264.7 cells at a concentration of 10 µM. Improved cell viability, along with reductions in intracellular MDA, ROS, and Fe^{2+} levels, was observed in the SiNPs + Fer-1 group relative to the corresponding levels in cells treated with SiNPs alone (Fig. 5A–D), indicating that Fer-1 effectively attenuated SiNPs-

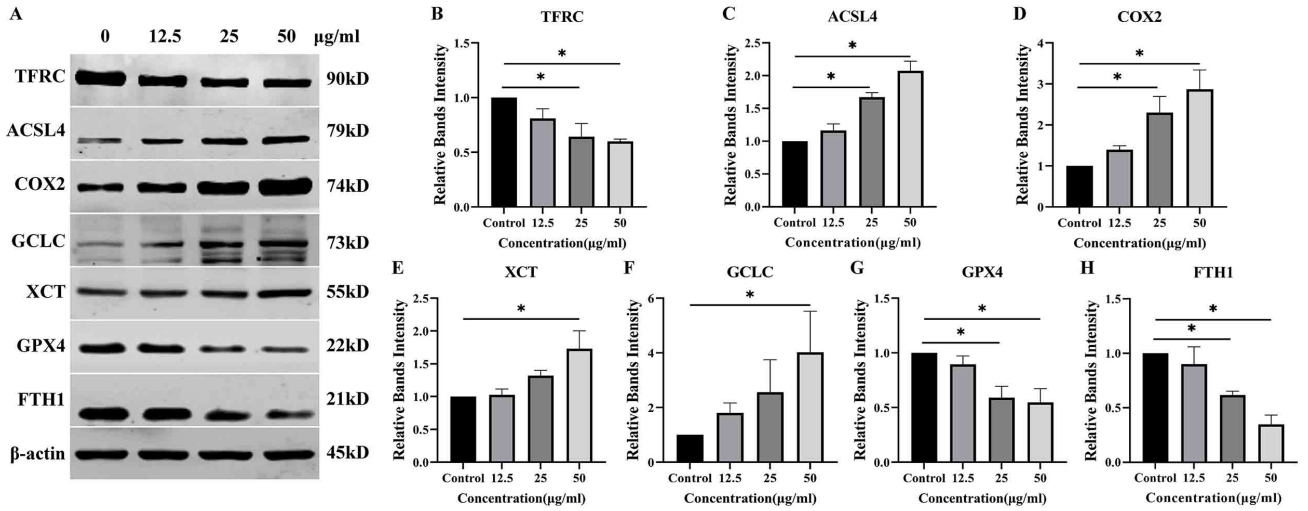

Fig. 4. SiNPs-induced changes in ferroptosis associated protein expression in RAW264.7 cells. (A) Western blotting images showing the expression of TFRC, ACSL4, COX2, GCLC, XCT, GPX4, and FTH1 in RAW264.7 cells treated with SiNPs (0, 12.5, 25, and 50 μg/mL) for 12 h. β-actin was used as a loading control. (B–H) Quantification of TFRC, ACSL4, COX2, XCT, GCLC, GPX4, and FTH1 protein expression levels normalized to β-actin. Data are presented as the mean ± standard deviation (SD; n = 3), and were analyzed using one-way ANOVAs followed by Bonferroni's post-hoc test. *$p < 0.05$ *vs*. control group.

induced oxidative stress and iron accumulation. Western blotting further demonstrated that, compared with the SiNPs treatment group, co-treatment with Fer-1 significantly restored GPX4 and FTH1 expression while suppressing ACSL4 and COX2 levels (Fig. 5E–I), collectively suggesting that Fer-1 effectively counteracted SiNPs-induced ferroptosis-related molecular alterations. These results confirm that Fer-1 partially reversed SiNPs-induced cellular injury in RAW264.7 cells, implicating lipid peroxidation-dependent ferroptosis as a central mechanism underlying SiNPs-related toxicity.

3.6 SiNPs Induce Cell Death Predominantly Through Ferroptosis in RAW264.7 Cells

To systematically evaluate the involvement of different cell death pathways in the phenotypes observed above, RAW264.7 cells were treated with the necroptosis inhibitor Nec-1 (10 μM), or the apoptosis inhibitor Z-VAD (10 μM) in combination with SiNPs exposure. Viability was then assessed via CCK-8 assay, revealing that Nec-1 and Z-VAD failed to effectively restore cell viability (Fig. 6A,B). Western blotting additionally showed that SiNPs increased the expression of MLKL, p-MLKL, and Cleaved-Caspase3. Although Nec-1 and Z-VAD treatment partially reduced the expression of MLKL/p-MLKL and Cleaved-Caspase3, respectively (Fig. 6C–G), these treatments did not markedly improve cell viability. These findings therefore suggest that ferroptosis, apoptosis, and necroptosis are all involved in SiNPs-induced cell death in RAW264.7 cells; however, ferroptosis appears to be the predominant mode of cell death following SiNPs exposure.

3.7 Global miRNA Expression Analysis

Global miRNA expression was next profiled in RAW264.7 cells treated with 0 or 50 μg/mL SiNPs, which were respectively designated as the Control and Experimental groups. Differentially expressed miRNAs (DEMs) identified when comparing these two groups were presented in a volcano plot (Fig. 7A). In this analysis, exposure to 50 μg/mL SiNPs was associated with 79 upregulated and 19 downregulated miRNAs (Fig. 7B). Hierarchical clustering heatmap analysis revealed distinct miRNA expression profiles between groups, with the right four columns representing control samples (C1–C4) and the left four columns representing experimental samples (M1–M4) (Fig. 7C). To explore the potential functional roles of the identified DEMs, GO and KEGG pathway enrichment analyses were conducted based on their predicted target genes (Fig. 7D–G).

To further refine the list of candidate miRNAs with relevant functional roles, DEMs were subjected to additional filtering using a stringent q-value < 0.05 threshold, yielding 8 significantly dysregulated miRNAs: mmu-miR-339-5p, mmu-miR-148a-3p, mmu-miR-100-5p, mmu-miR-381-3p, mmu-miR-3535, mmu-miR-677-3p, mmu-miR-6240, and mmu-miR-378c. Of these, mmu-miR-339-5p, mmu-miR-6240, and mmu-miR-677-3p were predicted to be involved in ferroptosis-related pathway regulation. Further comparison of their expression levels revealed that mmu-miR-339-5p exhibited the highest *baseMean* value (*baseMean* = 455), substantially exceeding that of both mmu-miR-6240 (*baseMean* = 51) and mmu-miR-677-3p (*baseMean* = 29), thus indicating that mmu-miR-339-5p was the most abundantly expressed of these three candidate DEMs in this experimental context. A review of the liter-

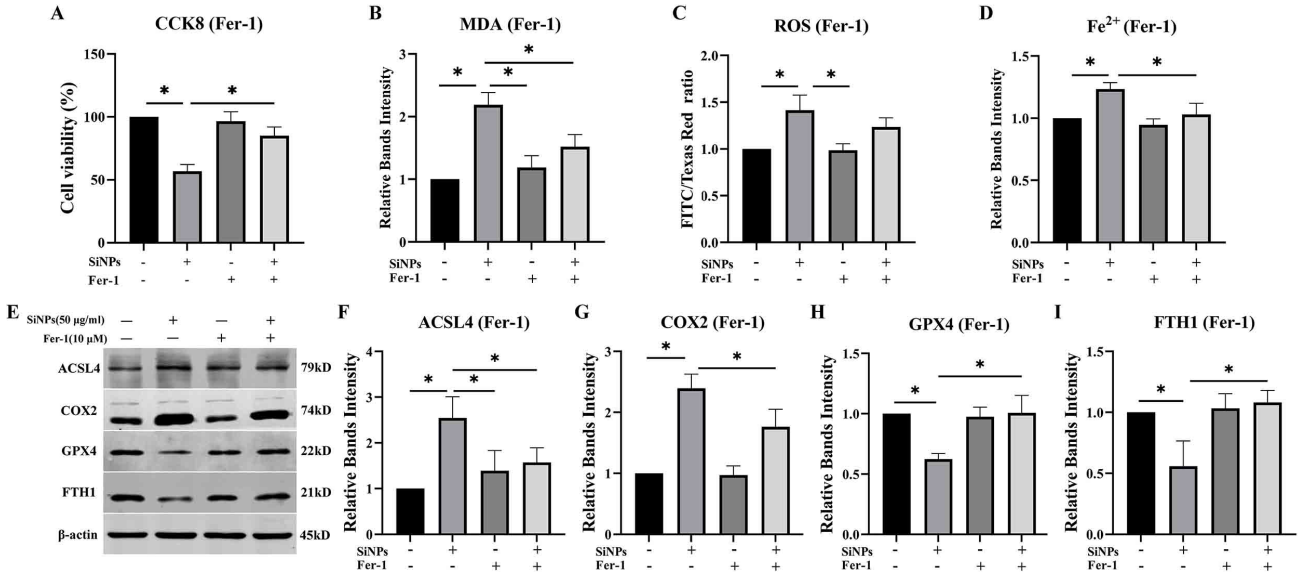

Fig. 5. Fer-1 attenuates SiNPs-induced ferroptosis. (A) Viability of cells treated with SiNPs (50 μg/mL) and/or the ferroptosis inhibitor Fer-1 (10 μM), as assessed by CCK-8 assay. (B–D) Results from assays used to detect MDA, lipid ROS (expressed as the FITC/Texas Red fluorescence ratio), and Fe^{2+} showing the levels of oxidative stress markers in cells treated with SiNPs and/or Fer-1. (E) Western blotting images showing the expression of ACSL4, COX2, GPX4, and FTH1 in cells treated with SiNPs (50 μg/mL) and/or Fer-1 (10 μM). β-actin was used as a loading control. (F–I) Quantification of ACSL4, COX2, GPX4, and FTH1 protein levels normalized to β-actin. Data are presented as the mean ± standard deviation (SD; n = 3), and were analyzed using one-way ANOVAs followed by Bonferroni's post-hoc test. *$p < 0.05$.

ature further revealed that only mmu-miR-339-5p has been previously reported to participate in the regulation of ferroptosis. Based on these criteria, miR-339-5p was selected as a target for further functional investigation.

3.8 miR-339-5p Regulates SiNPs-Induced Ferroptosis in RAW264.7 Cells

qRT-PCR analysis confirmed that miR-339-5p expression was markedly reduced in RAW264.7 cells upon SiNPs exposure, corroborating the miRNA sequencing data (Fig. 8A,B). To explore the functional role of this miRNA directly, cells were transfected with miR-339-5p mimics, resulting in efficient overexpression as verified by qRT-PCR. CCK-8 assay results demonstrated that miR-339-5p overexpression partially counteracted the SiNPs-induced reduction in cell viability (Fig. 8C), accompanied by a marked reduction in intracellular MDA levels, indicating the alleviation of lipid peroxidation (Fig. 8D). The expression of ferroptosis-associated proteins was additionally evaluated in this experimental context, revealing that ACSL4, a key determinant of lipid remodeling and ferroptosis susceptibility, was significantly downregulated in mimic-transfected cells, together with a pronounced reduction in COX2 expression (Fig. 8E–G).

Together, these results indicate that miR-339-5p plays a regulatory role in SiNPs-induced ferroptotic induction in RAW264.7 cells through the modulation of lipid metabolic pathways.

3.9 miR-339-5p Directly Targets Acsl4

To investigate whether *Acsl4* is a direct target of miR-339-5p, binding site prediction was performed using bioinformatics tools, revealing a putative miR-339-5p binding sequence within the 3′UTR of the *Acsl4* mRNA (Fig. 8H). To experimentally validate this interaction, luciferase reporter constructs carrying either the wild-type (WT) or mutant (Mut) *Acsl4* 3′UTR were generated and co-transfected with miR-339-5p mimics or negative control (NC) constructs. Luciferase activity was significantly reduced in cells carrying the *Acsl4*-WT construct upon miR-339-5p overexpression compared to the NC group, whereas mutation of the predicted binding site completely abolished this suppressive effect, with no significant difference observed between the miR-339-5p-OE and NC groups transfected with the *Acsl4*-Mut construct (Fig. 8I). These findings provide direct evidence that miR-339-5p binds to the 3′UTR of *Acsl4* in a sequence-specific manner, establishing *Acsl4* as a bona fide downstream target of miR-339-5p and suggesting that the regulatory effects of miR-339-5p on ferroptosis are mediated, at least in part, through its ability to directly repress *Acsl4* expression.

4. Discussion

The rapid commercialization and large-scale industrial production of SiNPs have contributed to a greater risk of occupational exposure and growing concerns surrounding associated health risks [1]. Unlike micron-sized

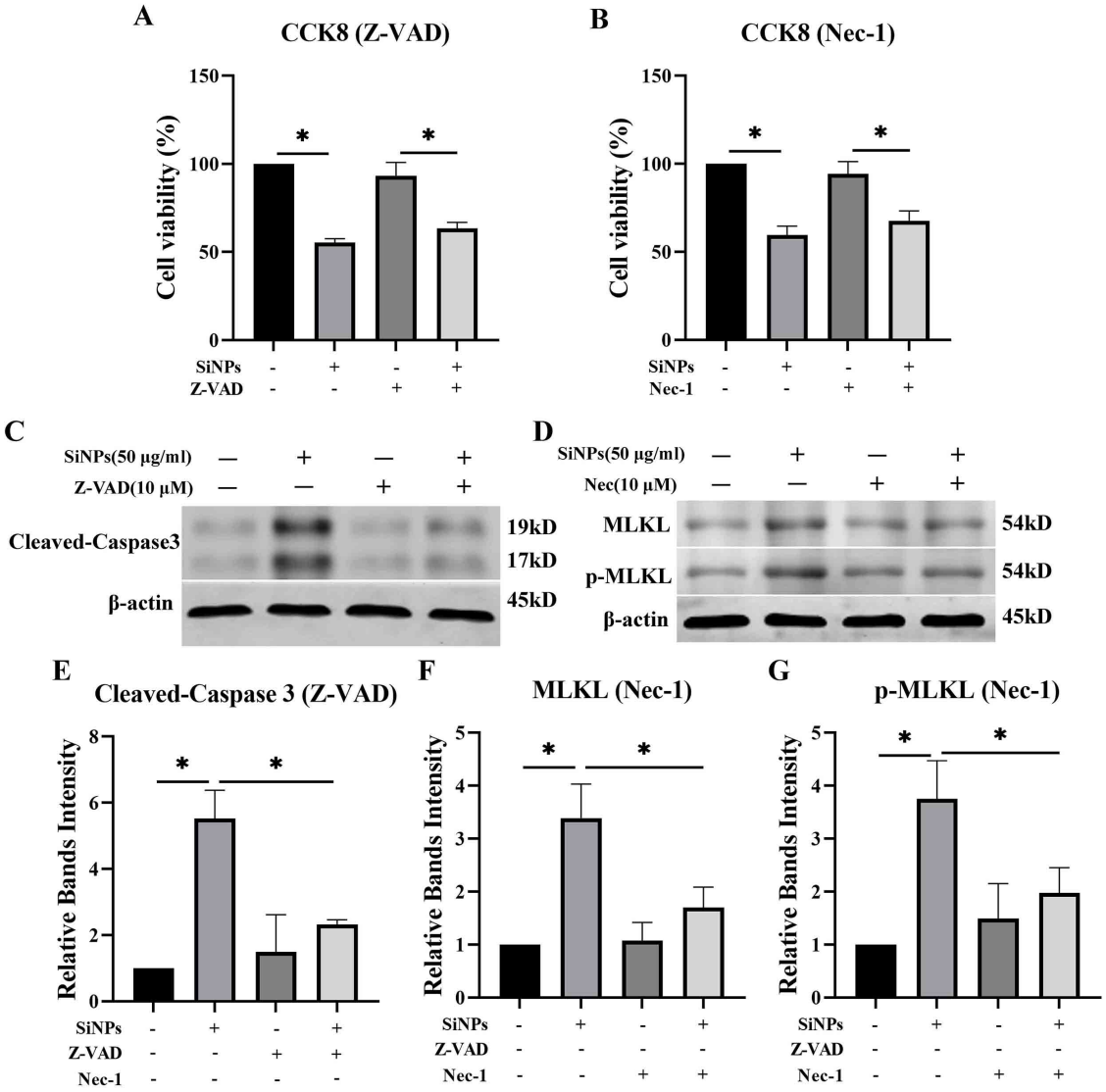

Fig. 6. SiNPs induce cell death predominantly through ferroptosis. (A,B) Viability of cells treated with SiNPs (50 μg/mL) and/or the necroptosis inhibitor Nec-1 (10 μM), or the apoptosis inhibitor Z-VAD (10 μM), as assessed by CCK-8 assay. (C) Western blotting images showing Cleaved-Caspase3 expression in cells treated with SiNPs (50 μg/mL) and/or Z-VAD (10 μM). β-actin was used as a loading control. (D) Western blotting images showing MLKL and p-MLKL expression in cells treated with SiNPs (50 μg/mL) and/or Nec-1 (10 μM). β-actin was used as a loading control. (E–G) Quantification of Cleaved-Caspase3, MLKL, and p-MLKL protein levels normalized to β-actin. Data are presented as the mean ± standard deviation (SD; n = 3), and were analyzed using one-way ANOVAs followed by Bonferroni's post-hoc test. *$p < 0.05$.

silica particles, the nanoscale dimensions of SiNPs allow them to penetrate more deeply into the respiratory tract, enabling alveolar deposition and necessitating a more concerted examination of their safety profile and potential adverse health consequences [40]. Although SiNPs have been implicated in the pathogenesis of PF, the underlying cellular and molecular mechanisms remain incompletely understood. Previous studies have predominantly focused on the roles that inflammation, autophagy, and cellular injury play in this context, whereas the functional importance of ferroptosis and miRNA-mediated regulation has received comparatively limited attention [41,42].

Ferroptosis is a regulated form of cell death defined by iron-dependent lipid peroxidation [29]. Many reports have implicated ferroptosis in various respiratory disorders, with current research focusing largely on its role in lung epithelial cells and the associated regulation of lung injury [43]. As central regulators of lung homeostasis, macrophages have, in parallel, been identified as promising targets for therapeutic intervention. In this study, we found that exposure to defined concentrations of SiNPs was sufficient to trigger ferroptosis in RAW264.7 cells, providing a framework to explore the underlying mechanistic basis for these deleterious effects.

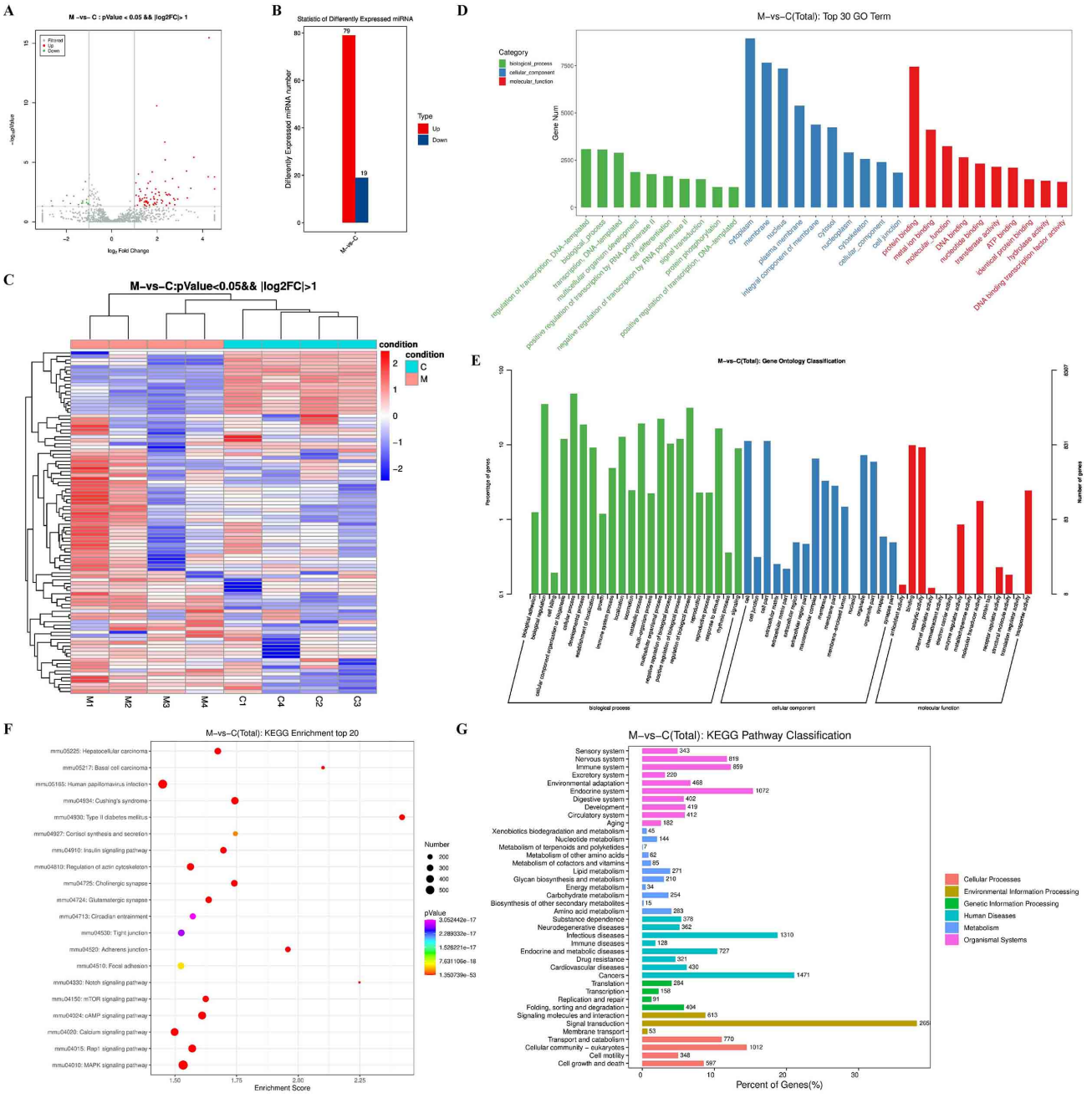

Fig. 7. miRNA sequencing and bioinformatics analysis. (A) Volcano plot showing the distribution of differentially expressed miRNAs (DEMs) between SiNPs-treated and control cells ($p < 0.05$ and |log2FC| >1). (B) Bar chart showing 79 upregulated (red) and 19 downregulated (blue) miRNAs following SiNPs exposure. (C) Hierarchical clustering heatmap of DEMs; the right four columns represent control samples (C1–C4) while the left four columns represent experimental samples (M1–M4). (D) The top 30 enriched GO terms for DEM target genes, categorized into biological processes (green), cellular components (blue), and molecular functions (red). (E) GO classification bar chart showing the distribution of DEM target genes across three categories. (F) Bubble plot of the top 20 enriched KEGG pathways, with bubble color reflecting statistical significance and bubble size denoting gene number. (G) KEGG pathway classification bar chart showing the distribution of DEM target genes across six functional categories.

We initially confirmed the detrimental impact of SiNPs on the viability of RAW264.7 cells. Cell viability assays revealed a time and dose-dependent decrease at 12 h and 24 h. While a transient increase in cell viability exceeding 100% was observed at 3 h and 6 h in cells exposed to low concentrations of SiNPs (6.25, 12.5, and 25 μg/mL), this phenomenon is likely attributable to a hormetic response, whereby low-dose nanoparticle exposure activates adaptive cellular stress responses rather than inducing cytotoxicity, a biphasic pattern previously documented for silver nanopar-

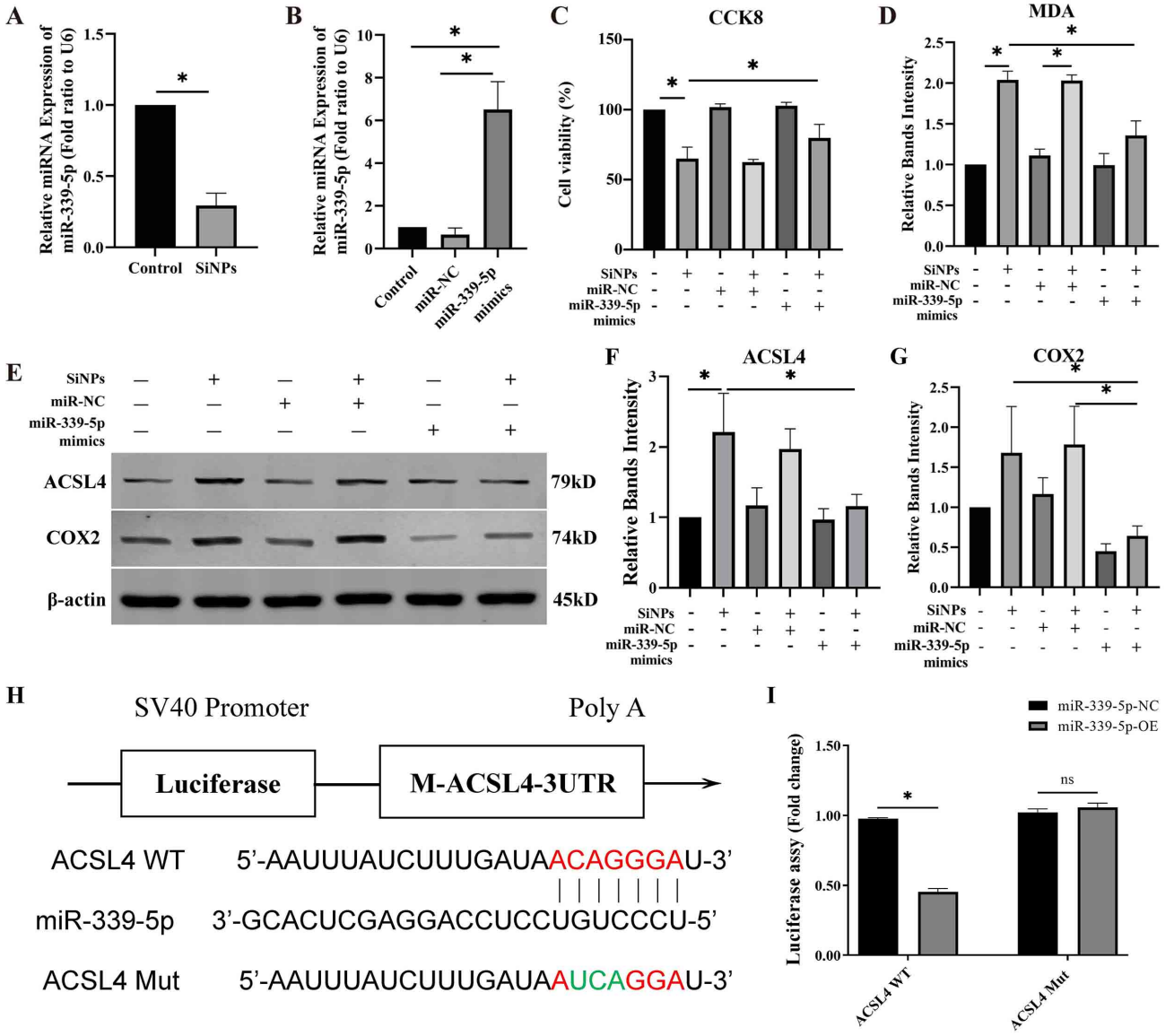

Fig. 8. miR-339-5p regulates SiNPs-induced ferroptosis by directly targeting *Acsl4* in RAW264.7 cells. (A) qRT-PCR analysis of miR-339-5p expression in RAW264.7 cells following SiNPs exposure (50 μg/mL, 12 h). (B) qRT-PCR verification of miR-339-5p mimics transfection efficiency. (C) Viability of SiNPs-exposed RAW264.7 cells transfected with miR-339-5p mimics or miR-NC as assessed by CCK-8 assay. (D) Intracellular MDA levels were measured in the indicated treatment groups. (E) Representative Western blotting images showing ACSL4 and COX2 protein levels, with β-actin as a loading control. (F,G) Quantitative analysis of ACSL4 and COX2 protein levels normalized to β-actin. (H) Schematic illustration of the predicted binding site shared between miR-339-5p and the 3′UTR of the *Acsl4* mRNA, including both wild-type (WT) and mutant (Mut) sequences. (I) Dual luciferase reporter assay confirming a direct interaction between miR-339-5p and the *Acsl4* 3′UTR; Luciferase activity was significantly reduced in cells carrying the *Acsl4*-WT construct upon miR-339-5p overexpression, whereas mutation of the binding site abolished this effect. Data are presented as the mean ± standard deviation (SD; n = 3), and were analyzed using one-way ANOVAs followed by Bonferroni's post-hoc test. *$p < 0.05$; ns, not significant.

ticles via MuD-mediated p38/ERK MAPK signaling [44]. At sub-toxic concentrations, SiNPs may stimulate mitochondrial activity by interacting with the outer mitochondrial membrane [45], resulting in enhanced mitochondrial dehydrogenase activity detected as increased absorbance in the CCK-8 assay [46]. With the prolongation of exposure time to 12 h and 24 h, or exposure to higher SiNP concentrations, progressive oxidative stress overwhelmed the defensive capacity of treated macrophages, leading to the dose- and time-dependent decline in cell viability that characterized overt cytotoxicity in our model. TEM revealed efficient uptake of SiNPs by RAW264.7 cells, accompanied

by mitochondrial ultrastructural alterations consistent with ferroptosis, including mitochondrial rounding, membrane condensation, and cristae loss [47]. These morphological observations were subsequently validated by western blotting analysis and lipid peroxidation measurements. SiNPs markedly downregulated GPX4, a central ferroptosis suppressor responsible for detoxifying lipid hydroperoxides, alongside FTH1, the major intracellular iron storage protein, while concurrently upregulating pro-ferroptotic mediators such as ACSL4 and COX2. Collectively, these results confirm that SiNPs exposure triggers ferroptosis in RAW264.7 cells.

The mechanistic basis for SiNPs-induced intracellular Fe^{2+} accumulation warrants further discussion. We observed the concurrent downregulation of both FTH1 and TFRC alongside significant Fe^{2+} accumulation in SiNPs-treated RAW264.7 cells, suggesting that multiple iron regulatory mechanisms are simultaneously dysregulated upon nanoparticle exposure. FTH1, the major intracellular iron storage protein, sequesters Fe^{3+} in a non-reactive form, and its downregulation is expected to release stored iron into the cytosolic labile pool, thereby increasing the availability of redox-active Fe^{2+} [48]. This mechanism is consistent with previous reports demonstrating that FTH1 degradation through ferritinophagy represents a critical step in ferroptosis initiation by mobilizing stored iron. The observed downregulation of TFRC upon SiNPs exposure is noteworthy, as it differs from the canonical upregulation of TFRC reported in most ferroptosis models. This paradoxical decrease may reflect a compensatory cellular response to counteract progressive iron overload, whereby cells attempt to limit further iron influx by suppressing transferrin receptor expression. However, this compensatory response appears insufficient to prevent the continued accumulation of labile iron and the ensuing lipid peroxidation, and the precise mechanism underlying TFRC downregulation in this context warrants further investigation. Beyond the regulation of iron storage and uptake, the pronounced mitochondrial structural alterations observed by TEM suggest that mitochondrial dysfunction may also contribute to intracellular iron dysregulation. Mitochondria are central hubs of iron utilization for heme and iron-sulfur cluster biosynthesis, and their structural disruption can impair iron processing, leading to mitochondrial iron accumulation and subsequent leakage of labile iron into the cytoplasm [49,50]. Taken together, SiNPs-induced Fe^{2+} accumulation in RAW264.7 cells is likely driven primarily by FTH1 downregulation-mediated release of stored iron, with mitochondrial dysfunction serving as an additional contributing factor, while TFRC downregulation may represent an insufficient compensatory attempt to limit iron overload. To further validate the role of ferroptosis in this context, we employed Fer-1, a classical ferroptosis inhibitor [51]. Fer-1 significantly increased GPX4 levels and decreased COX2 and ACSL4 levels, consistent with the alleviation of the ferroptosis process in RAW264.7 cells. This suggests that the occurrence of ferroptosis in these RAW264.7 cells is primarily mediated through the lipid peroxidation pathway. Notably, Fer-1 which acts at the execution stage of ferroptosis by directly inhibiting lipid peroxidation, effectively rescued SiNPs-induced cytotoxicity and ferroptosis-related molecular alterations. Therefore, the use of Fer-1 provides strong evidence supporting lipid peroxidation–dependent ferroptosis in this model.

In addition to ferroptosis, the potential involvement of apoptosis and necroptosis in SiNPs-induced cell death was also evaluated. Treatment with the apoptosis inhibitor Z-VAD and the necroptosis inhibitor Nec-1 failed to significantly rescue cell viability, despite partial reductions in Cleaved-Caspase3 and MLKL/p-MLKL expression, respectively. These findings suggest that while apoptotic and necroptotic signaling pathways are activated upon SiNPs exposure, they play subsidiary roles compared to ferroptosis in mediating SiNPs-induced cytotoxicity in RAW264.7 cells. The concurrent activation of multiple cell death pathways likely reflects the complexity of cellular responses to SiNPs, and the relative dominance of ferroptosis may be attributable to the pronounced iron accumulation and lipid peroxidation triggered by the internalization of these nanoparticles. Cross-talk between these pathways cannot be excluded, as shared upstream signals such as oxidative stress and mitochondrial dysfunction may simultaneously engage ferroptotic, apoptotic, and necroptotic cascades.

miRNAs have been identified as important regulators of ferroptosis and potential therapeutic targets for lung injury [36], but their roles as regulators of SiNPs-induced macrophage ferroptosis remain poorly understood. To address this gap, transcriptomic sequencing was performed on SiNPs-exposed RAW264.7 cells, and miR-339-5p was selected for further investigation based on its significant downregulation, its enrichment in ferroptosis-related pathways by KEGG analysis, and prior evidence implicating it in the regulation of ferroptosis across multiple diseases. In hepatocellular carcinoma, for instance, miR-339-5p has been reported to modulate intracellular iron levels through ATG7-mediated autophagic degradation of FTH1 [52], with elevated labile iron potentially playing a distinct tumor-suppressive function in this setting, highlighting the context-dependent nature of the regulatory role of miR-339-5p in ferroptotic induction. In ischemic tissue injury models, this miRNA has been further shown to activate the KEAP1/Nrf2 antioxidant axis to suppress ferroptosis [53], collectively suggesting that miR-339-5p is a multifaceted ferroptosis regulator operating through both iron homeostasis and redox signaling.

In the present study, overexpression of miR-339-5p in SiNPs-exposed RAW264.7 cells significantly reduced ACSL4 and COX2 protein expression and attenuated lipid peroxidation, demonstrating its functional role as a suppressor of ferroptotic induction. Bioinformatics predictions

identified *Acsl4* as a candidate target of miR-339-5p, and this interaction was directly validated by dual luciferase reporter assay, establishing *Acsl4* as a bona fide downstream target of miR-339-5p. ACSL4 promotes ferroptosis by esterifying polyunsaturated fatty acids into membrane phospholipids, thereby priming cells for lipid peroxidation [54], while COX2 serves as a downstream marker reflecting ferroptotic lipid oxidative stress. The direct targeting of *Acsl4* by miR-339-5p therefore provides a mechanistic explanation for the attenuation of lipid peroxidation and ferroptosis observed upon miR-339-5p overexpression in SiNPs-exposed RAW264.7 cells.

Among the multiple regulators of ferroptosis identified in this study, ACSL4 emerged as a pro-ferroptotic mediator that was markedly upregulated upon SiNPs exposure. ACSL4 is a critical executor of ferroptosis that catalyzes the esterification of polyunsaturated fatty acids, particularly arachidonic acid and adrenic acid, into membrane phospholipids, generating the lipid peroxide substrates that drive ferroptotic cell death [54]. Unlike GPX4, the downregulation of which reflects a more general cellular response to oxidative stress, ACSL4 represents an upstream and specific determinant of ferroptotic susceptibility, as its expression level is a primary determinant of the cellular capacity for lipid peroxidation. Genetic or pharmacological inhibition of ACSL4 confers resistance to ferroptosis across multiple cell types and disease models. ACSL4 knockout or blockade of its PKCβII-mediated phosphorylation at Thr328 has been shown to suppress ferroptosis *in vitro* and *in vivo* [55], and direct pharmacological targeting of ACSL4 with AS-252424 similarly attenuated lipid peroxidation and ferroptosis in diverse cell lines and organ injury models [56], underscoring the central role of ACSL4 in ferroptosis execution. In our study, the marked upregulation of ACSL4 upon SiNPs exposure, combined with the direct confirmation that miR-339-5p targets the 3′UTR of ACSL4 by dual luciferase reporter assay, positions the miR-339-5p/ACSL4 axis as a pivotal regulatory mechanism governing SiNPs-induced ferroptosis in macrophages. Furthermore, the observed reductions in both ACSL4 protein expression and lipid peroxidation markers upon miR-339-5p overexpression provide functional evidence that this axis is not merely associative but mechanistically operative in this model.

While ferroptosis is regulated at multiple interconnected levels, the present data provide a rationale for prioritizing the miR-339-5p/ACSL4 axis as the predominant regulatory mechanism in this model. With respect to GPX4-mediated redox control, our data confirm that GPX4 protein expression was significantly downregulated at the protein level upon SiNPs exposure (Fig. 4). However, GPX4 downregulation in this context likely reflects a downstream consequence of oxidative stress amplification rather than the primary initiating event. Notably, the concurrent upregulation of GCLC and XCT observed in our study suggests that the glutathione synthesis and cystine/glutamate antiporter systems are transcriptionally activated as compensatory antioxidant responses to counteract SiNPs-induced oxidative stress. This compensatory induction, while insufficient to prevent ferroptosis execution, underscores the complexity of the redox regulatory network engaged by SiNPs and indicates that System Xc^--dependent GSH replenishment may represent an additional layer of ferroptosis regulation in this model, underscoring the need for further investigation. With respect to iron homeostasis, our data demonstrate that SiNPs exposure significantly elevated intracellular Fe^{2+} levels while also downregulation of FTH1 and TFRC, indicating concurrent dysregulation of iron storage and uptake mechanisms (Figs. 2,4). As noted above, FTH1 downregulation-mediated release of stored iron into the labile pool likely constitutes a primary driver of Fe^{2+} accumulation, with mitochondrial dysfunction serving as an additional contributing factor. Importantly, although iron dyshomeostasis is an indispensable prerequisite for ferroptosis, it is not specifically targeted by miR-339-5p in our model. Rather, the elevated labile iron pool provides the redox-active substrate that, in conjunction with ACSL4-mediated PUFA-phospholipid enrichment of the membrane, drives the lipid peroxidation cascade to lethal levels. In this sense, iron dysregulation and the miR-339-5p/ACSL4 axis operate as complementary and potentially synergistic mechanisms that together amplify SiNPs-induced ferroptosis, rather than competing alternatives.

Together, these results demonstrate that miR-339-5p protects against SiNPs-induced macrophage cytotoxicity by suppressing ferroptosis through the downregulation of ACSL4, identifying it as a key modulator of ferroptosis in this context and reinforcing the central role of lipid peroxidation in SiNPs-mediated macrophage injury. The upstream mechanisms governing SiNPs-induced miR-339-5p downregulation remain to be fully elucidated, and may involve oxidative stress, loss of iron homeostasis, and inflammatory signaling, highlighting key areas for further investigation.

5. Limitations

Despite these promising findings, several limitations to the present study should be acknowledged. First, this study was conducted exclusively *in vitro* using RAW264.7 cells, and this system does not fully recapitulate the complex pathophysiology of SiNPs-induced lung injury *in vivo*. Therefore, the observed regulatory effects of miR-339-5p on ferroptosis require further validation in appropriate animal models. Second, the upstream regulatory mechanisms governing miR-339-5p expression upon SiNPs exposure remain to be fully elucidated and warrant further investigation.

6. Conclusions

This study demonstrates that SiNPs induce ferroptosis in RAW264.7 macrophages by dysregulating lipid peroxi-

dation, iron homeostasis, and antioxidant defense systems. Mechanistically, SiNPs exposure downregulates miR-339-5p, thereby relieving its suppression of ACSL4 and enhancing lipid peroxidation-dependent ferroptosis. These findings identify the miR-339-5p/ACSL4 axis as a key regulatory node in the SiNPs-induced activation of ferroptotic signaling, providing a molecular basis for the development of strategies aimed at mitigating nanomaterial-induced macrophage injury.

Abbreviations

SiNPs, Silica Nanoparticles; miRNAs, microRNAs; Fer-1, Ferrostatin-1; Nec-1, Necrostatin-1; GO, Gene Ontology; KEGG, Kyoto Encyclopedia of Genes and Genomes; ROS, Reactive oxygen species; MDA, Malondialdehyde; qRT-PCR, quantitative real-time polymerase chain reaction; TEM, Transmission electron microscopy.

Availability of Data and Materials

All data contained in the study are available from the corresponding author on reasonable request.

Author Contributions

WZ and HS designed the research study. WZ performed the research. WZ, YL, ZD and HS actively participated in the experimental procedures and data analysis. WZ wrote the manuscript. All authors contributed to editorial changes in the manuscript. All authors read and approved the final manuscript. All authors have participated sufficiently in the work and agreed to be accountable for all aspects of the work.

Ethics Approval and Consent to Participate

Not applicable.

Acknowledgment

The Graphical Abstract figure support was provided by Figdraw.

Funding

This research was funded by the National Key Research and Development Program of China (No. 2022YFC250320), National Natural Science Foundation of China (NSFC) (No. 81602893 and No. 81872575), Natural Science Foundation of Shandong Province (No. ZR2021MH218 and No. ZR2022MH184); Shandong Province Medical and Health Technology Development Plan (No. 202312010854); Shandong Province Traditional Chinese Medicine Science and Technology Plan (No. Z-2023114), and Jinan Science and Technology Plan (No. 202328074).

Conflicts of Interest

The authors declare no conflicts of interest.

References

[1] Huang Y, Li P, Zhao R, Zhao L, Liu J, Peng S, et al. Silica nanoparticles: Biomedical applications and toxicity. Biomedicine & Pharmacotherapy. 2022; 151: 113053. https://doi.org/10.1016/j.biopha.2022.113053

[2] Auffan M, Rose J, Bottero JY, Lowry GV, Jolivet JP, Wiesner MR. Towards a definition of inorganic nanoparticles from an environmental, health and safety perspective. Nature Nanotechnology. 2009; 4: 634–641. https://doi.org/10.1038/nnano.2009.242

[3] Mebert AM, Baglole CJ, Desimone MF, Maysinger D. Nanoengineered silica: Properties, applications and toxicity. Food and Chemical Toxicology. 2017; 109: 753–770. https://doi.org/10.1016/j.fct.2017.05.054

[4] Lee JA, Kim MK, Song JH, Jo MR, Yu J, Kim KM, et al. Biokinetics of food additive silica nanoparticles and their interactions with food components. Colloids and Surfaces. B, Biointerfaces. 2017; 150: 384–392. https://doi.org/10.1016/j.colsurfb.2016.11.001

[5] Morais RP, Hochheim S, de Oliveira CC, Riegel-Vidotti IC, Marino CEB. Skin interaction, permeation, and toxicity of silica nanoparticles: Challenges and recent therapeutic and cosmetic advances. International Journal of Pharmaceutics. 2022; 614: 121439. https://doi.org/10.1016/j.ijpharm.2021.121439

[6] Thabet AF, Boraei HA, Galal OA, El-Samahy MFM, Mousa KM, Zhang YZ, et al. Silica nanoparticles as pesticide against insects of different feeding types and their non-target attraction of predators. Scientific Reports. 2021; 11: 14484. https://doi.org/10.1038/s41598-021-93518-9

[7] Xu H, Zhu Y, Zhu L, Wang D, Lv S, Li X, et al. Warning on the inhalation of silica nanoparticles: Experimental evidence for its easy passage through the air-blood barrier, resulting in systemic distribution and pathological injuries. Chemico-biological Interactions. 2025; 409: 111423. https://doi.org/10.1016/j.cbi.2025.111423

[8] Setyawati MI, Singh D, Krishnan SPR, Huang X, Wang M, Jia S, et al. Occupational Inhalation Exposures to Nanoparticles at Six Singapore Printing Centers. Environmental Science & Technology. 2020; 54: 2389–2400. https://doi.org/10.1021/acs.est.9b06984

[9] Han HY, Cho JW, Seong E, Park EJ, Lee GH, Kim DW, et al. Amorphous silica nanoparticle-induced pulmonary inflammatory response depends on particle size and is sex-specific in rats. Toxicology and Applied Pharmacology. 2020; 390: 114890. https://doi.org/10.1016/j.taap.2020.114890

[10] Yin H, Fang L, Wang L, Xia Y, Tian J, Ma L, et al. Acute Silica Exposure Triggers Pulmonary Inflammation Through Macrophage Pyroptosis: An Experimental Simulation. Frontiers in Immunology. 2022; 13: 874459. https://doi.org/10.3389/fimmu.2022.874459

[11] Shi L, Zhang L, Ma Z, Hu Z, Geng Z, Liu H, et al. H3K18 lactylation drives the progression of silica nanoparticles-induced pulmonary fibrosis via promoting macrophage M1 polarization. Journal of Hazardous Materials. 2025; 496: 139286. https://doi.org/10.1016/j.jhazmat.2025.139286

[12] Li Y, Xu H, Wang Y, Zhu Y, Xu K, Yang Z, et al. Epithelium-derived exosomes promote silica nanoparticles-induced pulmonary fibroblast activation and collagen deposition via modulating fibrotic signaling pathways and their epigenetic regulations. Journal of Nanobiotechnology. 2024; 22: 331. https://doi.org/10.1186/s12951-024-02609-y

[13] Miao C, Jia P, Luo C, Pang J, Xiao L, Zhang T, et al. The size-dependent in vivo toxicity of amorphous silica nanoparticles: A systematic review. Ecotoxicology and Environmental Safety. 2024; 271: 115910. https://doi.org/10.1016/j.ecoenv.2023.115910

[14] Klein CL, Wiench K, Wiemann M, Ma-Hock L, van Ravenzwaay B, Landsiedel R. Hazard identification of inhaled nanomaterials: making use of short-term inhalation studies. Archives of Toxicology. 2012; 86: 1137–1151. https://doi.org/10.1007/s00204-012-0834-2
[15] Aegerter H, Lambrecht BN, Jakubzick CV. Biology of lung macrophages in health and disease. Immunity. 2022; 55: 1564–1580. https://doi.org/10.1016/j.immuni.2022.08.010
[16] Hou F, Shi N, Yuan H, Li B, Xiao J, Xiao K, et al. Targeting alveolar macrophages: a promising intervention for pulmonary infection and acute lung injury. Cellular & Molecular Biology Letters. 2025; 30: 69. https://doi.org/10.1186/s11658-025-00750-6
[17] Su R, Song L, Liu Y, Zhang C, Xie L, Han Z. Macrophage-Fibroblast Crosstalk in Fibrosis: Key Regulator of Fibrosis Across Different Organs. Frontiers in Bioscience (Landmark Edition). 2025; 30: 38864. https://doi.org/10.31083/fbl38864
[18] Zhang M, Wan Z, Zhu Z, Wang P, Xu X, Ma T, et al. A Comparative Study of the Effects of Nine CXCR3 Antagonists on Macrophage Function and the Treatment of Acute Lung Injury. Frontiers in Bioscience (Landmark Edition). 2025; 30: 45931. https://doi.org/10.31083/fbl45931
[19] Pervizaj-Oruqaj L, Ferrero MR, Matt U, Herold S. The guardians of pulmonary harmony: alveolar macrophages orchestrating the symphony of lung inflammation and tissue homeostasis. European Respiratory Review. 2024; 33: 230263. https://doi.org/10.1183/16000617.0263-2023
[20] Kulle A, Thanabalasuriar A, Cohen TS, Szydlowska M. Resident macrophages of the lung and liver: The guardians of our tissues. Frontiers in Immunology. 2022; 13: 1029085. https://doi.org/10.3389/fimmu.2022.1029085
[21] Inoue M, Sakamoto K, Suzuki A, Nakai S, Ando A, Shiraki Y, et al. Size and surface modification of silica nanoparticles affect the severity of lung toxicity by modulating endosomal ROS generation in macrophages. Particle and Fibre Toxicology. 2021; 18: 21. https://doi.org/10.1186/s12989-021-00415-0
[22] Nakayama M. Macrophage Recognition of Crystals and Nanoparticles. Frontiers in Immunology. 2018; 9: 103. https://doi.org/10.3389/fimmu.2018.00103
[23] Yang M, Jing L, Wang J, Yu Y, Cao L, Zhang L, et al. Macrophages participate in local and systemic inflammation induced by amorphous silica nanoparticles through intratracheal instillation. International Journal of Nanomedicine. 2016; 11: 6217–6228. https://doi.org/10.2147/IJN.S116492
[24] Li Y, Yao Q, Xu H, Ren J, Zhu Y, Guo C, et al. Lung Single-Cell Transcriptomics Offers Insights into the Pulmonary Interstitial Toxicity Caused by Silica Nanoparticles. Environment & Health. 2024; 2: 786–801. https://doi.org/10.1021/envhealth.4c00052
[25] Joshi GN, Knecht DA. Silica phagocytosis causes apoptosis and necrosis by different temporal and molecular pathways in alveolar macrophages. Apoptosis. 2013; 18: 271–285. https://doi.org/10.1007/s10495-012-0798-y
[26] Hamilton RF, Jr, Thakur SA, Holian A. Silica binding and toxicity in alveolar macrophages. Free Radical Biology & Medicine. 2008; 44: 1246–1258. https://doi.org/10.1016/j.freeradbiomed.2007.12.027
[27] Cheng P, Li S, Chen H. Macrophages in Lung Injury, Repair, and Fibrosis. Cells. 2021; 10: 436. https://doi.org/10.3390/cells10020436
[28] Yang G, Yang Y, Liu Y, Liu X. Regulation of alveolar macrophage death in pulmonary fibrosis: a review. Apoptosis: an International Journal on Programmed Cell Death. 2023; 28: 1505–1519. https://doi.org/10.1007/s10495-023-01888-4
[29] Jiang X, Stockwell BR, Conrad M. Ferroptosis: mechanisms, biology and role in disease. Nature Reviews. Molecular Cell Biology. 2021; 22: 266–282. https://doi.org/10.1038/s41580-020-00324-8
[30] Liang D, Minikes AM, Jiang X. Ferroptosis at the intersection of lipid metabolism and cellular signaling. Molecular Cell. 2022; 82: 2215–2227. https://doi.org/10.1016/j.molcel.2022.03.022
[31] Hu Y, Huang Y, Zong L, Lin J, Liu X, Ning S. Emerging roles of ferroptosis in pulmonary fibrosis: current perspectives, opportunities and challenges. Cell Death Discovery. 2024; 10: 301. https://doi.org/10.1038/s41420-024-02078-0
[32] Pei Z, Qin Y, Fu X, Yang F, Huo F, Liang X, et al. Inhibition of ferroptosis and iron accumulation alleviates pulmonary fibrosis in a bleomycin model. Redox Biology. 2022; 57: 102509. https://doi.org/10.1016/j.redox.2022.102509
[33] Lee J, Arisi I, Puxeddu E, Mramba LK, Amicosante M, Swaisgood CM, et al. Bronchoalveolar lavage (BAL) cells in idiopathic pulmonary fibrosis express a complex pro-inflammatory, pro-repair, angiogenic activation pattern, likely associated with macrophage iron accumulation. PloS One. 2018; 13: e0194803. https://doi.org/10.1371/journal.pone.0194803
[34] Kishore A, Petrek M. Roles of Macrophage Polarization and Macrophage-Derived miRNAs in Pulmonary Fibrosis. Frontiers in Immunology. 2021; 12: 678457. https://doi.org/10.3389/fimmu.2021.678457
[35] Jin S, Liu PS, Zheng D, Xie X. The interplay of miRNAs and ferroptosis in diseases related to iron overload. Apoptosis. 2023; 29: 45–65. https://doi.org/10.1007/s10495-023-01890-w
[36] Zhang WY, Wen L, Du L, Liu TT, Sun Y, Chen YZ, et al. S-RBD-modified and miR-486-5p-engineered exosomes derived from mesenchymal stem cells suppress ferroptosis and alleviate radiation-induced lung injury and long-term pulmonary fibrosis. Journal of Nanobiotechnology. 2024; 22: 662. https://doi.org/10.1186/s12951-024-02830-9
[37] Qi Z, Liu R, Ju H, Huang M, Li Z, Li W, et al. microRNA-130b-3p Attenuates Septic Cardiomyopathy by Regulating the AMPK/mTOR Signaling Pathways and Directly Targeting ACSL4 against Ferroptosis. International Journal of Biological Sciences. 2023; 19: 4223–4241. https://doi.org/10.7150/ijbs.82287
[38] Sun L, He X, Kong J, Yu H, Wang Y. Menstrual blood-derived stem cells exosomal miR-let-7 to ameliorate pulmonary fibrosis through inhibiting ferroptosis by Sp3/HDAC2/Nrf2 signaling pathway. International Immunopharmacology. 2024; 126: 111316. https://doi.org/10.1016/j.intimp.2023.111316
[39] Vranic S, Watanabe E, Yamazaki K, Wakahara T, Miyakawa K, Takeuchi S, et al. Impact of surface functional group modification on cellular internalization and cytotoxicity of silica nanoparticles. Particle and Fibre Toxicology. 2025; 23: 9. https://doi.org/10.1186/s12989-025-00653-6
[40] Mohammadpour R, Yazdimamaghani M, Cheney DL, Jedrzkiewicz J, Ghandehari H. Subchronic toxicity of silica nanoparticles as a function of size and porosity. Journal of Controlled Release. 2019; 304: 216–232. https://doi.org/10.1016/j.jconrel.2019.04.041
[41] Wang M, Li J, Dong S, Cai X, Simaiti A, Yang X, et al. Silica nanoparticles induce lung inflammation in mice via ROS/PARP/TRPM2 signaling-mediated lysosome impairment and autophagy dysfunction. Particle and Fibre Toxicology. 2020; 17: 23. https://doi.org/10.1186/s12989-020-00353-3
[42] Ma Y, Liang Q, Wang F, Yan K, Sun M, Lin L, et al. Silica nanoparticles induce pulmonary autophagy dysfunction and epithelial-to-mesenchymal transition via p62/NF-κB signaling pathway. Ecotoxicology and Environmental Safety. 2022; 232: 113303. https://doi.org/10.1016/j.ecoenv.2022.113303
[43] Liu P, Feng Y, Li H, Chen X, Wang G, Xu S, et al. Ferrostatin-1 alleviates lipopolysaccharide-induced acute lung injury via inhibiting ferroptosis. Cellular & Molecular Biology Letters. 2020; 25: 10. https://doi.org/10.1186/s11658-020-00205-0

[44] Choi JH, Min WK, Gopal J, Lee YM, Muthu M, Chun S, et al. Silver nanoparticle-induced hormesis of astroglioma cells: A Mu-2-related death-inducing protein-orchestrated modus operandi. International Journal of Biological Macromolecules. 2018; 117: 1147–1156. https://doi.org/10.1016/j.ijbiomac.2018.05.234

[45] Bressan E, Ferroni L, Gardin C, Rigo C, Stocchero M, Vindigni V, et al. Silver nanoparticles and mitochondrial interaction. International Journal of Dentistry. 2013; 2013: 312747. https://doi.org/10.1155/2013/312747

[46] Dowding JM, Song W, Bossy K, Karakoti A, Kumar A, Kim A, et al. Cerium oxide nanoparticles protect against Aβ-induced mitochondrial fragmentation and neuronal cell death. Cell Death and Differentiation. 2014; 21: 1622–1632. https://doi.org/10.1038/cdd.2014.72

[47] Stockwell BR, Friedmann Angeli JP, Bayir H, Bush AI, Conrad M, Dixon SJ, et al. Ferroptosis: A Regulated Cell Death Nexus Linking Metabolism, Redox Biology, and Disease. Cell. 2017; 171: 273–285. https://doi.org/10.1016/j.cell.2017.09.021

[48] Mancias JD, Wang X, Gygi SP, Harper JW, Kimmelman AC. Quantitative proteomics identifies NCOA4 as the cargo receptor mediating ferritinophagy. Nature. 2014; 509: 105–109. https://doi.org/10.1038/nature13148

[49] Battaglia AM, Chirillo R, Aversa I, Sacco A, Costanzo F, Biamonte F. Ferroptosis and Cancer: Mitochondria Meet the "Iron Maiden" Cell Death. Cells. 2020; 9: 1505. https://doi.org/10.3390/cells9061505

[50] Wu T, Liang X, Liu X, Li Y, Wang Y, Kong L, et al. Induction of ferroptosis in response to graphene quantum dots through mitochondrial oxidative stress in microglia. Particle and Fibre Toxicology. 2020; 17: 30. https://doi.org/10.1186/s12989-020-00363-1

[51] Miotto G, Rossetto M, Di Paolo ML, Orian L, Venerando R, Roveri A, et al. Insight into the mechanism of ferroptosis inhibition by ferrostatin-1. Redox Biology. 2020; 28: 101328. https://doi.org/10.1016/j.redox.2019.101328

[52] Cao F, Hao W, Liang W, Zeng H, Zheng J. MiR-339-5p Inhibits Ferroptosis by Promoting Autophagic Degradation of FTH1 Through Targeting ATG7 in Liver Cancer Cells. Clinical Medicine Insights. Oncology. 2024; 18: 11795549241244783. https://doi.org/10.1177/11795549241244783

[53] Yu G, Chen Y, Yang N, Zhang H, Zhang X, Geng Y, et al. Apoptotic Bodies Derived from Fibroblast-Like Cells in Subcutaneous Connective Tissue Inhibit Ferroptosis in Ischaemic Flaps via the miR-339-5p/KEAP1/Nrf2 Axis. Advanced Science. 2024; 11: e2307238. https://doi.org/10.1002/advs.202307238

[54] Doll S, Proneth B, Tyurina YY, Panzilius E, Kobayashi S, Ingold I, et al. ACSL4 dictates ferroptosis sensitivity by shaping cellular lipid composition. Nature Chemical Biology. 2017; 13: 91–98. https://doi.org/10.1038/nchembio.2239

[55] Zhang HL, Hu BX, Li ZL, Du T, Shan JL, Ye ZP, et al. PKCβII phosphorylates ACSL4 to amplify lipid peroxidation to induce ferroptosis. Nature Cell Biology. 2022; 24: 88–98. https://doi.org/10.1038/s41556-021-00818-3

[56] Huang Q, Ru Y, Luo Y, Luo X, Liu D, Ma Y, et al. Identification of a targeted ACSL4 inhibitor to treat ferroptosis-related diseases. Science Advances. 2024; 10: eadk1200. https://doi.org/10.1126/sciadv.adk1200